*(Received 27 November 2025, Accepted 25 December 2025, Scheduled 14 January 2026)*

# Multispectral Optical Emission Modeling of Sprites Using Plasma Streamer Simulations: A Computational Electromagnetics Approach for Remote Sensing Applications

Carlos Gómez* and Francisco Román

*Universidad Nacional de Colombia, Colombia*

**ABSTRACT:** We present a computational framework for the multispectral synthesis of optical emissions in Transient Luminous Events (TLEs), specifically sprites, based on plasma fluid simulations obtained using the `Afivo Streamer` tool. Using the simulated electric field and electron density, we computed quasi-stationary excitation, quenching, and radiative emission rates for four key spectral bands: first positive $1PN_2$ and second positive $2PN_2$ band systems of nitrogen, the Lyman-Birge-Hopfield (LBH) band system, and optical emission images of Ionized Atomic Oxygen at 777.4 nm (O I 777.4 nm). The model incorporates electron-impact excitation coefficients $k(E/N)$, non-radiative losses due to collisional quenching $Q = \sum_i \alpha_i n_i$, and atmospheric attenuation (especially relevant for LBH). It also produces 2D emission maps and vertical brightness profiles, showing the spatial localization of each band as a function of the reduced electric field, electron density, and non-radiative losses. The results capture the temporal evolution of the discharge, from the early propagation phase to advanced branching, enabling direct comparisons with spaceborne instrumentation (e.g., Atmosphere-Space Interactions Monitor-ASIM). The developed scheme provides a reproducible diagnostic tool that links physical plasma variables with the observed signals across multiple spectral bands.

## 1. INTRODUCTION

Transient Luminous Events (TLEs) in particular sprites are mesospheric electrical discharges whose characterization requires a multispectral approach. Although the $1PN_2$ (visible) band has been traditionally used to validate simulations through photographic and satellite observations [1, 2], other emissions such as $2PN_2$ (near-UV), Lyman-Birge-Hopfield (LBH) system (far-UV), and O I line at 777.4 nm are sensitive to different energy regimes and de-excitation processes, providing additional information on the dynamics of the ionization front, active chemistry, and electronic structure of the plasma [3, 4].

The recent development of multichannel instrumentation, particularly on satellite platforms, such as the Atmosphere-Space Interactions Monitor (ASIM) module onboard the International Space Station [5], has created the need for numerical models capable of consistently reproducing multiple optical bands to enable meaningful comparisons with observations. In this study, we present a multispectral computational framework built on plasma fluid simulations performed with the `Afivo Streamer` [6], in which excitation, quenching, and radiative emission rates are derived under a quasi-stationary approximation.

This approximation is justified by a strong separation of the time scales between the effective lifetimes of the excited states: $\tau_{\text{eff}} \sim 10^{-9}$–$10^{-6}$ s [7], and the characteristic time over which the macroscopic structure of the streamer evolves owing to propagation and expansion, referred to as the hydrodynamic time scale $\tau_{\text{dyn}}$. In the high-field streamer head region, which dominates the optical emission, effective lifetimes are typically at the lower end of this range because of the strong radiative decay and quenching.

The hydrodynamic time can be estimated as $\tau_{\text{dyn}} \sim R_{\text{head}}/v_{\text{head}} \gtrsim 10^{-6}$–$10^{-4}$ s, typically for sprite streamer head radii $R_{\text{head}} \sim 200$–$500$ m and propagation velocities $v_{\text{head}} \sim 10^6$–$10^7$ m s$^{-1}$ [8]. Since $\tau_{\text{eff}} \ll \tau_{\text{dyn}}$, temporal derivatives of excited-state populations can be neglected without loss of accuracy, and the emitted radiation directly traces the instantaneous reduced electric field and electron density. This provides a physically consistent basis for multispectral diagnostics of streamer discharges. We note that this approximation is not intended to describe long-lived afterglow emissions dominated by slow chemical processes, but is well suited for excitation-dominated optical emissions in active streamer regions.

Initially implemented for $1PN_2$, the model was extended to $2PN_2$, LBH, and O I at 777 nm, incorporating the relevant atmospheric attenuation in the FUV [9] and the specific kinetic dependencies of each transition. This allows the generation of maps and vertical profiles that are comparable to instrumentation data, and supports the analysis of the spectral localization of emissions as a function of reduced field, electron density, and non-radiative losses.

The central objective was to provide a reproducible optical synthesis scheme capable of directly linking plasma physical variables to the observed signals in different bands, thus enabling its use as a diagnostic tool. In the following sections, we

* Corresponding author: Carlos Gómez (cagomezv@unal.edu.co).

describe the methodology and present multispectral results that capture both early streamer propagation and its evolution into branched regimes, laying the groundwork for direct comparison with satellite observations.

## 2. FRAMEWORK AND METHODOLOGY

This section presents the computational workflow used to obtain the time series of emissions in $1PN_2$, $2PN_2$, LBH, and O I 777.4 nm from the plasma simulation results. The electric-field magnitude $|\vec{E}|$ and electron density $n_e$ were interpolated onto an $(x, y)$ grid, and the reduced field $E/N$ was evaluated using an exponential profile for the neutral density $N(y)$ and molar fractions for $N_2$, $O_2$, and O. Given $E/N$, the excitation coefficients were obtained from the tabulated data and used to compute the excited-state population $n_k$. The apparent radiance was obtained by line-of-sight integration, incorporating atmospheric transmittance where relevant (particularly for LBH in the FUV).

The initial implementation focused on emissions from the $1PN_2$ system. In this case, collisional quenching was dominated by collisions with $N_2$, with the contribution of $O_2$ being negligible. This simplifies the modeling of non-radiative losses and reduces the number of required parameters. In addition, the excitation coefficients $k(E/N)$ for $1PN_2$ are well documented in databases such as LXCat [10], which increases the robustness and numerical stability of the interpolation during post-processing. Based on these results, the model was extended to the aforementioned emission lines.

### 2.1. Excitation Coefficients $k(E/N)$

The electron-impact excitation coefficient curves $k(E/N)$ for the spectral bands of interest ($2PN_2$, $1PN_2$, LBH, and O I 777 nm) are shown in Fig. 1. These curves, derived from Boltzmann solvers in the LXCat database [10], represent the probability of exciting each transition as a function of the reduced electric field. The steep rise below ∼200 Td reflects the energy threshold of each process, whereas saturation or decay at a higher $E/N$ indicates reduced efficiency. For example, the O I 777 nm band (red dashed curve) shows an overall lower efficiency, consistent with its higher excitation threshold (∼10.7 eV). These dependencies directly modulate the calculated emission intensity, and higher $E/N$ values produce higher excitation rates $\nu_k$.

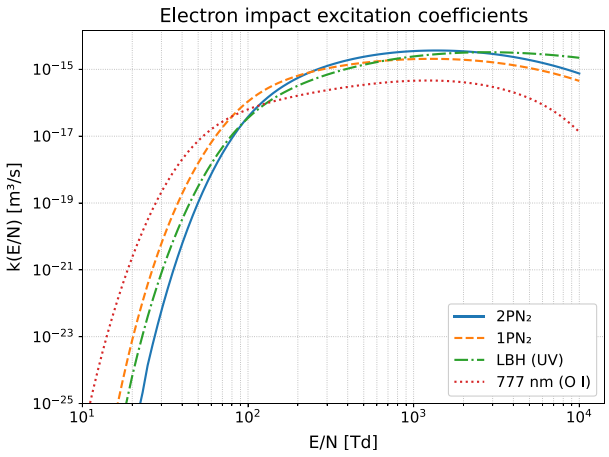


**FIGURE 1**. Electron-impact excitation coefficients $k(E/N)$ for the main radiative channels considered: Second Positive ($2PN_2$), First Positive ($1PN_2$), LBH (UV), and atomic oxygen at 777 nm.

In practice, these functions are interpolated to assign a local excitation frequency $\nu_k$ to each grid point $\nu_k(E/N) = k(E/N)N$, where $N$ is the local neutral density.

### 2.2. Post-Processing Framework for Optical Emissions

In the $1PN_2$ system, energetic electrons in the plasma excite nitrogen molecules ($N_2$) into the metastable triplet electronic state $B^3\Pi_g$ [11]. In this excited state, the molecules can follow two main de-excitation pathways:

i) a transition to a lower vibrational level of the electronic ground state ($X^1\Sigma_g^+$) via photon emission, that is, *fluorescence* or *radiative emission* [12], characterized by the radiative rate $A$; and

ii) non-radiative de-excitation through collisions (*quenching*) with neutral molecules present in the plasma [13], primarily $N_2$ and $O_2$, a process described by a collisional quenching rate [14].

The balance between these processes determines the quantum efficiency or radiative yield, which represents the fraction of excited molecules that contribute to the observed optical emission in this system [15]. Thus, the procedure for computing the optical emission intensities involves the following steps:

1. Interpolate $|\vec{E}|$ and $n_e$ from the simulation results, construct $N(y)$, and compute the reduced electric field $E/N$ using an exponential profile for the neutral density $N(y)$, defined as

$$N(y) = N_0 \exp\left(-\frac{y - y_0}{H}\right), \tag{1}$$

where $H$ is the scale height, $y_0$ the reference altitude, and $N_0$ the reference density, respectively.

2. The excitation coefficient specific to the transition $k_k(E/N)$ for each band was interpolated and the excitation frequency $\nu_k(E/N)$ was evaluated from the curves in Fig. 1.

$$\nu_k = N(y) \cdot k_k(E/N).$$

3. Evaluate the density of the excited state:

$$n_k \approx \frac{\nu_k\, n_e}{A_k + Q_k},$$

where $A_k$ is the radiative decay rate, and $Q_k$ is the collisional quenching rate given by $Q = \sum_i \alpha_i n_i$, where $\alpha_i$ is the quenching coefficient for species $i$, and $n_i$ is the number density.

4. The optical emission was integrated along the vertical direction to obtain column-integrated brightness in Rayleigh. The volumetric emission (in photons per unit volume and time) is given by:

$$I_k = A_k \cdot n_k.$$

**TABLE 1**. Kinetic and radiative parameters for excited states relevant to multispectral emissions. Values are approximate and representative of mesospheric conditions.

| Transition/State | $\lambda$ [nm] | $A$ ($s^{-1}$) | $\alpha_1$ ($m^3/s$) | $\alpha_2$ ($m^3/s$) | Quenching Species | Source |
|---|---|---|---|---|---|---|
| $1PN_2$ | 650–900 | $1.7 \times 10^5$ | $1.0 \times 10^{-17}$ | $3.0 \times 10^{-16}$ | $N_2$ | [1, 24] |
| $2PN_2$ | 337–380 | $2.0 \times 10^7$ | $1.0 \times 10^{-17}$ | $3.0 \times 10^{-16}$ | $N_2$, $O_2$ | [1, 24] |
| LBH ($N_2$) | 150–280 | $1.8 \times 10^4$ | $1.0 \times 10^{-17}$ | $1.0 \times 10^{-16}$ | $O_2$, $O_3$ | [1, 24] |
| O I (777 nm) | 777.4 | $4.0 \times 10^7$ | $5.9 \times 10^{-16}$ | $1.1 \times 10^{-15}$ | O, $O_2$, $N_2$ | [25] |

To express it in optical units, such as *Rayleigh* units, it is integrated along the line of sight (*LOS*):

$$B_k = \frac{10^{-6}}{4\pi} \int_{\text{LOS}} I_k ds,$$

where $ds$ is the differential element along the optical path.

The optical synthesis procedure was implemented using a `Python` script that processes the `.vtk` files generated by the plasma simulations. From these outputs, the code interpolates the electron density $n_e$ and electric-field magnitude $|\vec{E}|$ onto a regular grid to apply the calculations described in the previous section. In this study, the simulation was performed using a fluid model based on a *drift-diffusion-reaction* framework under *Local Field Approximation (LFA)*, as described in [16] and Appendix A. This script generates multiple visualization products, including vertical emission profiles, 2D emission maps, electron density maps, and electric field maps, which are independently applied to each pixel in the 2D grid. Adapting the scheme to different spectral bands only requires updating the band-specific parameters $A_k$, $\nu_k(E/N)$, and $Q_k$ for each transition.

Transient Luminous Events (TLEs) produce emissions spanning from the far-ultraviolet to the near-infrared region [17]. To study these phenomena and their influence on the atmosphere and climate system, the European Space Agency (ESA), in collaboration with DTU Space (Denmark), deployed the *Atmosphere-Space Interactions Monitor* (ASIM) at the International Space Station (ISS) [5]. ASIM comprises two main modules: (i) the *Modular Multispectral Imaging Array* (MMIA), which includes two cameras and three photometers to observe emissions in the ultraviolet, visible, and near-infrared regions, and (ii) the *Modular X- and Gamma-ray Sensor* (MXGS), which detects X and $\gamma$ rays in the approximate range of 15 keV to 20 MeV.

The MMIA optical module operates at wavelengths associated with relevant mesospheric plasma transitions: one camera (CHU1) centered at 337.0 nm ($2PN_2$ system), another (CHU2) centered at 777.4 nm (O I line), and three high-speed photometers (∼100 kHz) at 337 nm, LBH (180–230 nm), and 777.4 nm [18]. This instrumental configuration has a direct correspondence with the $2PN_2$ (near-UV), LBH (far-UV), and O I 777.4 nm emissions considered in this study, enabling direct comparison between simulations and satellite data.

The extension implemented here provides complementary information related to the $2PN_2$ band, which dominates the upper regions of sprites and is sensitive to the reduced field and energy of accelerated electrons [4]. Additionally, the intensity ratio $2PN_2/1PN_2$ can be used to estimate $E/N$ [19]. The LBH band, requires explicit treatment of atmospheric absorption by $O_2$ and $O_3$, as it is strongly attenuated in the far-UV region and is therefore critical for accurately modeling the apparent brightness observed from satellite platforms [9]. In the developed script, this effect was incorporated through a band-averaged attenuation factor applied along the vertical line of sight.

O I 777.4 nm line is associated with high-energy electrons and the dissociative processes of oxygen. The O I triplet at 777.4 nm represents one of the most important radiative contributions in oxygen — containing plasmas. The upper levels of the associated transitions are easily populated (excitation energy of approximately 10.7 eV) and have a significant Einstein coefficient (of the order $4 \times 10^7$ $s^{-1}$). Therefore, the triplet can be used for plasma diagnostics, that is, to determine the electron temperature ($T_e$) and density ($n_e$), in the absence of detectable hydrogen lines in the spectrum [20].

From an observational standpoint, $2PN_2$ (337–380 nm) and O I (777 nm) are good tracers of fine structures owing to their short radiative lifetimes. The $1PN_2$ band (650–900 nm) offers a robust signal and is less affected by atmospheric attenuation, making it suitable for use with instruments in the visible region. The LBH band (FUV) requires the application of the atmospheric transmission factor $T_{\text{atm}}$ owing to absorption by $O_2$ and, where appropriate, $O_3$ [21]. Because of the large absorption cross sections of molecular oxygen in the Schumann-Runge continuum, small variations in atmospheric composition, temperature, or viewing geometry can lead to significant uncertainty in $T_{\text{atm}}$, particularly for nadir observations of LBH emissions [9, 22]. The sensitivity of far-UV transmittance to atmospheric variability and geometry is a well-known feature of ultraviolet radiative transfer and is discussed in standard radiative transfer studies, which show that uncertainties in atmospheric profiles can result in large variations in the effective ultraviolet (UV) transmittance [23].

Table 1 summarizes the specific parameters for the four emitters ($1PN_2$, $2PN_2$, LBH, and O I 777 nm): the spectral range, Einstein radiative coefficient $A$, and bimolecular quenching coefficient $\alpha_i$ for the dominant species.

## 3. MULTIBAND EMISSION MAPS AND TEMPORAL PROFILES

At each time step, the numerical routine generates two-dimensional emission maps (expressed in Rayleigh) for each spectral band, together with the corresponding electron density

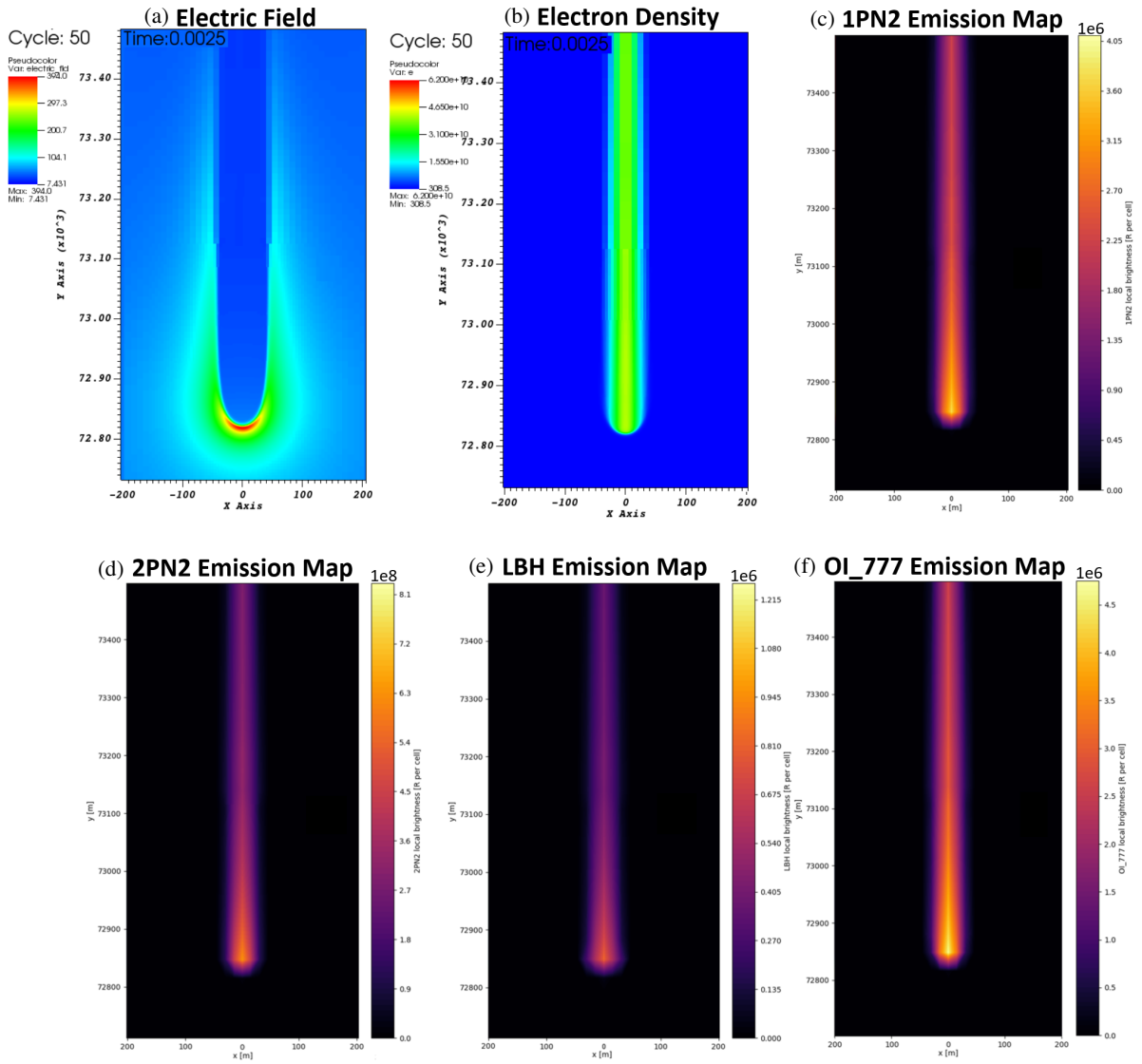


**FIGURE 2**. Distribution maps of the simulated streamer front at $t = 2.5$ ms. (a) Reduced electric field $E/N$, showing intensification at the streamer head with values exceeding 200 Td. (b) Electron density $n_e$, revealing the conductive channel established behind the front. (c)–(f) Optical emission maps in Rayleighs for the bands: $1PN_2$ (337 nm), $2PN_2$, LBH (150–200 nm), and O I 777 nm. Emissions are mainly concentrated in the head region, while $1PN_2$ and $2PN_2$ exhibit extension along the ionized channel. The LBH band includes a band-averaged vertical atmospheric attenuation, which reduces contributions from lower layers.

and electric field. Vertical profiles of column-integrated brightness were computed on the same grid to compare the spatial extent and localization of emissions among the spectral bands. Longitudinal profiles of the electric field and emission along the symmetry axis ($x = 0$) were also extracted. These results can be directly compared to satellite observations or ground-based measurements. Similar multispectral diagnostics have been reported in optical and spectrophotometric observations of sprites and streamer discharges, where the emission morphology and relative band localization are used as primary validation criteria [4, 5, 7, 9]. As an example, Fig. 2 shows the streamer discharge front at $t = 2.5$ ms, where we display: (a) the electric field map, (b) the electron density, and (c)–(f) the optical emission maps for the $1PN_2$ (337 nm), $2PN_2$, LBH (UV, 150–200 nm), and O I 777 nm channels.

Figure 2(a) shows the *electric field* map. A localized intensification is observed at the streamer head, approximately between 72.8 and 73.0 km altitude, where the reduced field reaches values above 200 Td. This region has a nearly hemispherical geometry, with strong gradients that decay rapidly in the radial direction. The maximum-field zone aligns with the channel axis, forming a well-collimated, well-defined front. Such a localized enhancement of $E/N$ at the streamer head is a well-established feature of sprite streamers inferred from optical observations and supported by streamer theory [4, 26]. In this region, the reduced field $E/N$ exceeds the ionization and excitation thresholds of the neutral gas, activating the processes responsible for the production of electrons and excited species, which in turn generate optical emission in the channel body (downstream of the propagating front).

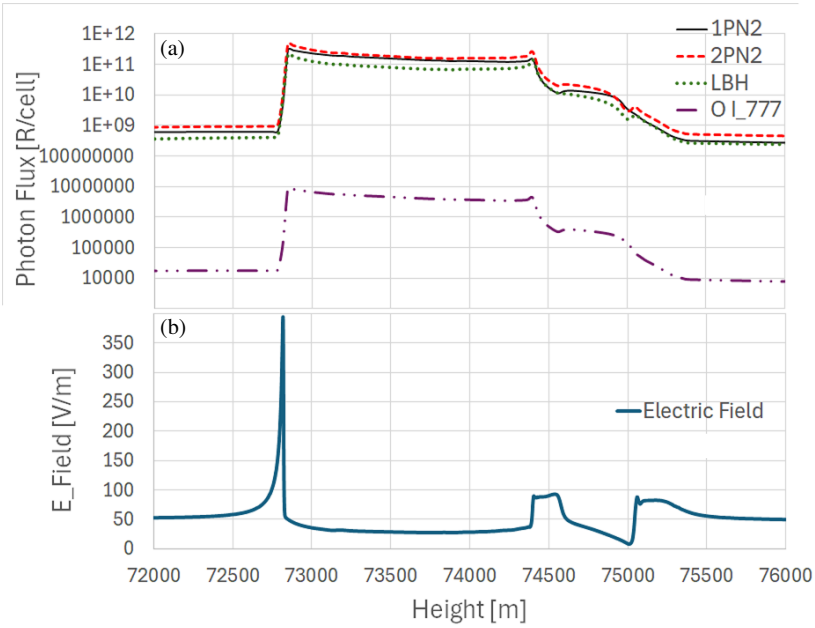


**FIGURE 3**. Co-located vertical profiles at a given instant (e.g., $t = 2.5$ ms). (a) Local brightness contribution (Rayleighs/cell) in four bands. (b) Electric field distribution along the symmetry axis as a function of discharge altitude.

Figure 2(b) shows the *electron density* map. The conductive channel already established behind the streamer head is evident, with densities of the order of $10^{10}$ m$^{-3}$. The distribution was axially symmetric with a narrow core, which was consistent with the early propagation stage. Comparable channel widths and electron density levels have been inferred from sprite modeling constrained by ISUAL and ground-based observations, supporting the realism of the simulated channel structure [7, 27]. The contrast between the head (where the reduced field intensifies, and avalanche ionization dominates) and the channel (where the conductivity increases and the field collapses) reflects the nonlinear nature of the streamer ionization dynamics [26, 27].

Figures 2(c)–(f) display the *multispectral emission* maps, that is, the radiation generated in different bands as a result of electronic excitation. The 1PN$_2$ band was concentrated in the head region and extended into the immediate channel with reduced sensitivity to atmospheric attenuation. This spatial distribution is consistent with observations showing that 1PN$_2$ emissions provide a robust tracer of the streamer body in both satellite and ground-based imaging [4, 7].

The 2PN$_2$ band exhibited a somewhat more extended longitudinal structure, and, given its short radiative lifetime, it acted as a fine tracer of the active front region. Such confinement of 2PN$_2$ emission to the high-field region is consistent with spectrophotometric measurements and has been widely used as a diagnostic tool for streamer heads in sprites [7, 19].

The LBH band (FUV) appears comparatively more diffuse, combining production near the head with upstream and downstream contributions. This implementation includes a vertical band-averaged atmospheric transmission $T_{\text{atm}} = \exp(-\tau)$, such that the relative signal from the lower layers is attenuated by oxygen absorption (mainly $O_2$ and, where modeled, $O_3$). This behavior is consistent with previous modeling and ISUAL observations, which reported strong attenuation and reduced apparent brightness of LBH emissions under nadir viewing geometry [9, 28].

Finally, the O I 777 nm line is associated with the excitation of atomic oxygen. Its intensity tends to correlate with regions of higher electron energy and is particularly prominent in leader-type processes in lightning spectra [29], whereas it can be weaker or intermittent in sprites. Satellite measurements indicate that when present, O I 777 nm emission is typically localized near the streamer head and exhibits peak irradiances comparable to those reproduced by the present simulations [5].

Overall, the results showed spatial consistency among the electric field, electron density, and optical emission. The ionized channel behind the head sustains conduction, while each spectral band emphasizes different aspects of the phenomenon: the high-field head concentrates the emission at 2PN$_2$ and O I 777 nm, 1PN$_2$ traces the persistence of the channel, and the LBH band reflects both radiative production and FUV absorption. The agreement of these spatial patterns with published emission maps and spectrophotometric diagnostics supports the applicability of the model for remote sensing interpretations of streamer-type discharges.

### 3.1. Emission Profiles

Figure 3(a) shows the radiation profiles for the four bands (1PN$_2$, 2PN$_2$, LBH, and O I 777 nm) as a function of altitude at $t = 2.5$ ms. Fig. 3(b) shows the electric field profile along the same vertical cut ($x = 0$), as a reference to locate the main brightness centers.

The local contribution to the brightness (in Rayleighs per cell) for a given transition $k$ is written in the code as

$$I_{\text{loc}}(y) = 10^{-6}\, A n_k(y) \Delta y,$$

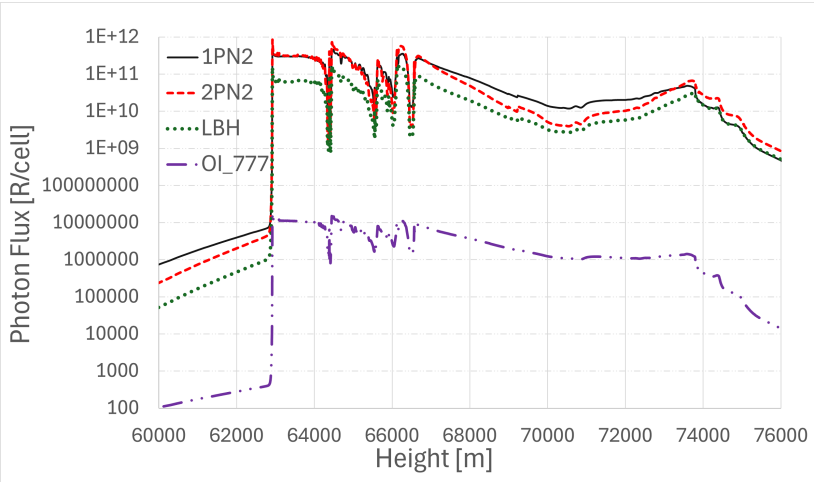


**FIGURE 4**. Vertical profiles of local brightness $I_{\text{loc}}$ in Rayleighs per cell (R/cell) for $1PN_2$, $2PN_2$, LBH, and O I 777 nm, at $t = 12.5$ ms.

where $A$ is the Einstein coefficient for spontaneous emission [$s^{-1}$]; $n_k$ is the density of the excited state responsible for emission [$m^{-3}$]; and $\Delta y$ is the cell thickness along the line of sight (LOS). Factors $10^{-6}$ convert photon flux into Rayleigh units [30]. Under quasi-stationary conditions, the local signal can be expressed as:

$$I_{\text{loc}}(y) = 10^{-6}\, A n_k(y) \Delta y$$
$$\propto \frac{A}{A + Q(y)}\, k\left(\frac{E}{N}(y)\right) n_{\text{target}}(y) n_e(y) \qquad (2)$$

where $n_{\text{target}}$ is the density of the target species to be excited (e.g., $N_2$, O, $O_2$) [$m^{-3}$]. The factor $A/(A+Q)$ represents the radiative fraction: if $Q \gg A$, quenching dominates and emission is suppressed; if $Q \ll A$, nearly the entire population in state $k$ decays radiatively [31]. The factor $k(E/N)$ controls the excitation efficiency and increases sharply when $E/N$ exceeds the transition threshold, which explains why the maxima of $I_{\text{loc}}$ coincide with the $E/N$ peaks at the streamer head. The product $n_e\, n_{\text{target}}$ sets the volumetric rate of effective collisions, where $n_e$ is larger (head and immediate channel), and there is more production of $n_k$. In this way, it becomes clear that $N_2$ bands ($1PN_2$ and $2PN_2$) dominate the channel brightness, whereas LBH reproduces the morphology but is attenuated by atmospheric transmission $T_{\text{atm}}(\lambda)$. The O I 777 nm emission is several orders of magnitude smaller because of its dependence on atomic oxygen and strong quenching in dense layers. Overall, the figure illustrates how the product $k(E/N)\, n_e$ at the head controls the brightness, whereas $A/(A+Q)$ and $T_{\text{atm}}$ modulate the differences between bands.

A piecewise analysis of the profiles revealed three clear regions along the vertical axis:

i) Between 72.8 and 73 km, all bands exhibited a simultaneous, abrupt increase over several orders of magnitude, which coincided with the intersection of the streamer head with the vertical cut, where the electric field reached its maximum ($|\mathbf{E}| \sim 350$–$370$ V/m). At this point, the head concentrates most of the instantaneous brightness, and $E/N$ and $n_e$ reach their maxima. Owing to the steep slope of $k(E/N)$ in the 100–300 Td range (Fig. 1), the emission grows explosively.

ii) Between 73 and 74.5 km, there is a plateau with a gentle decay, characteristic of the conductive channel left by the streamer front. In this region, the electron density decreases slowly, and $E/N$ remains at moderate values, which explains the gradual decay of $I_{\text{loc}}$. The factor $\frac{A}{A+Q}$, which regulates the radiative fraction against quenching, plays a key role in shaping the slope of each band. Small inflections (e.g., near 74.4 km) reveal local re-intensifications of the field; and

iii) above 74.5 km all bands show a pronounced drop as the discharge enters a low-$E/N$, low-density region, where quenching dominates.

We observe that the $2PN_2$ band (red segmented line) is the most intense in the channel, followed by $1PN_2$ (black solid line), and LBH (green dotted line). This is consistent with the following: (a) favorable thresholds and cross-sections for $2PN_2$ at the head, (b) a somewhat lower radiative efficiency $\frac{A}{A+Q}$ for $1PN_2$ at these altitudes, and (c) FUV attenuation experienced by LBH along the line of sight, such that even with a source similar to $1PN_2$, its signal appears more suppressed. The O I 777 nm line (violet dashed-dotted line) is several orders of magnitude below. At this time, the fraction of atomic oxygen was small, and the main production mechanism was the dissociative channel $e^- + O_2 \rightarrow O(5P) + O$, which contributed appreciably only at the head. In addition, quenching by $N_2/O_2$ is highly efficient, which explains the rapid decay after the peak.

### 3.2. Advanced Discharge State, $t = 12.5$ ms

At a later time, $t = 12.5$ ms, the front advanced, and the streamer entered a branched regime. The local emission is still governed by $I_{\text{band}} \propto [A/(A+Q)] k(E/N) n_{\text{target}} n_e$, but the field and current are now distributed among several tips. In Fig. 4, a pronounced jump is observed in the vertical profiles of the local brightness $I_{\text{loc}}$ near an altitude of ~63 km, which marks

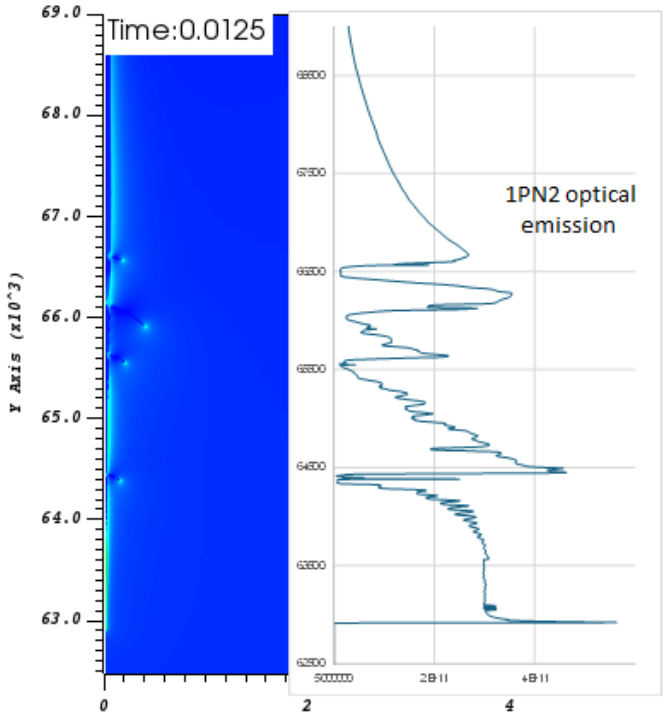


**FIGURE 5**. Space-altitude correlation at $t = 12.5$ ms. Left: electric field map (color scale) showing local maxima associated with the streamer head and several sub-heads due to branching. Right: vertical $1PN_2$ emission profile (R/cell) in the same column; peaks and plateaus align with the bright structures in the field map.

the streamer head where $k(E/N)$ is maximal. Above that altitude, a slowly decaying plateau appears, which is associated with the already formed conductive channel. Repeated peaks and notches emerge between ∼64 and 66.5 km, corresponding to sub-heads and branches that share the field and generate narrower local maxima. At heights near ∼73–74 km, a secondary enhancement was observed, followed by a global decay as $E/N$ and $n_e$ decreased.

The relative intensity order remains the same: $N_2$ bands dominate because of their larger excitation coefficients and more favorable radiative fractions $\frac{A}{A+Q}$ [32]. In contrast, LBH appeared weaker because of the accumulated FUV absorption along the line of sight. O I 777 nm emission is several orders of magnitude smaller and exhibits a smoother morphology. Its intensity depends on the local availability of atomic oxygen and excitation/dissociation at the streamer head, which explains the sharp increase at the head altitude, followed by a broad plateau with less pronounced variations than those in the $N_2$ lines. This band responds with a higher sensitivity to the abundance of O and the radiative fraction, which improves slightly at higher altitudes. Consequently, the decay along the channel was less abrupt. However, it shows a pronounced drop once the discharge leaves the region where the electric field is sufficient to dissociate the atmospheric oxygen molecules [4].

Overall, the profile is consistent with a *branched* regime, that is, multiple narrow peaks (sub-heads) superimposed on an extended background (channel), each leaving a tail immediately above. Between the peaks, the signal remained at intermediate levels owing to the integrated contribution of the already formed conductive channel. The amplitude of the main peak is smaller than at $t = 2.5$ ms because the available potential is distributed among several tips and the maximum field at each is reduced by screening.

The superposition of the electric field map and radiation profile is shown in Fig. 5. There is a one-to-one correlation between the maxima in the radiation profile and the branching structures in the field map. Each bifurcation generates a local emission maximum at the same altitude, whereas the absolute maximum of the profile is located at the main-streamer head (around ∼63 km).

The appearance of multiple peaks in $1PN_2$ at $t = 12.5$ ms is consistent with the simulations, which indicate that the front begins to branch around ∼9.5 ms. Once branching starts, the brightness of the main head ceases to increase, and secondary peaks emerge, co-located with the new branches. The distance traveled by each tip between successive instants decreases, reflecting the charge motion that accumulates at the tips of the more conductive branches [33].

### 3.3. Spatial Profiles of $1PN_2$ Emission

Figure 6 shows the vertical profiles of $1PN_2$ emissions several times during the discharge. At all times, a sharp peak appears at the lowest altitudes, associated with the streamer head where the reduced field $E/N$ and electron density $n_e$ reach their maxima. At higher altitudes, the signal decreases and forms a tail that reflects the conductive channel left by the front and the radiative and collisional relaxation of the excited states.

Each curve exhibits a pronounced step that moves towards lower altitudes as time progresses (from ∼74–75 km at $t = 2.5$ ms to ∼61–62 km at $t = 17.1$ ms), marking the streamer head. Behind this step, a decaying plateau appeared, which was associated with the already formed conductive channel. At heights between ∼64 and 66.5 km, narrow peaks and notches (more evident at $t = 10$–$15$ ms) are observed, indicative of front branching and the emergence of sub-heads that redistribute the field. Later, as the head descends into denser layers, quenching ($Q$) increases, reducing the radiative fraction and causing the background level of the profile to decay more rapidly.

In the interval $t \approx 2.5$–$5$ ms, the head peak increases and shifts to higher altitudes: the product $k(E/N)n_e$ at the tip grows and, as the head rises, the neutral density decreases, reducing $Q$ and improving the radiative efficiency $A/(A+Q)$. The evolution is consistent with a well-focused head sustained by a sufficiently high background field. At $t \approx 7.5$ ms, the peak drops sharply. This minimum can be explained by: (i) field screening due to accumulated space charge and head broadening (which reduces $E/N$), (ii) a transient decrease in $n_e$ ahead of the tip due to reduced photoionization, and (iii) possible departure from the region of maximum background field. Because $k(E/N)$ has a steep slope, a moderate reduction in $E/N$ is sufficient to significantly reduce the excitation, even if $Q$ decreases.

Between $t = 10$ and 17 ms, the peak partially recovered because of the reorganization of the reduced field $E/N$ associated

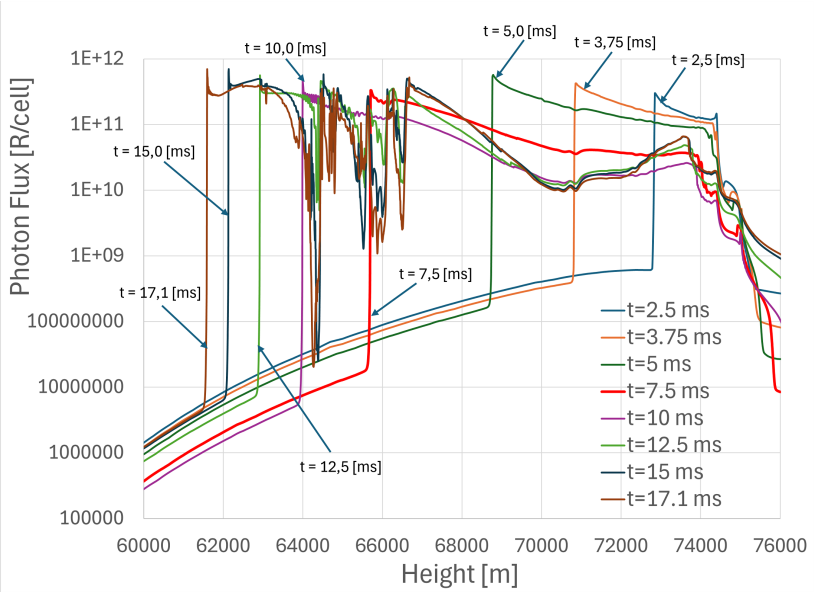


**FIGURE 6**. Temporal evolution of local photon flux for the $1PN_2$ band as a function of altitude (horizontal axis in meters). The vertical axis shows photon flux in Rayleighs per cell (R/cell). Profiles at different times ($t = 2.5$–$17.1$ ms) are superimposed. Abrupt jumps mark the position of the streamer head at each time, while fine oscillations between ∼64–66.5 km correspond to sub-heads and branching.

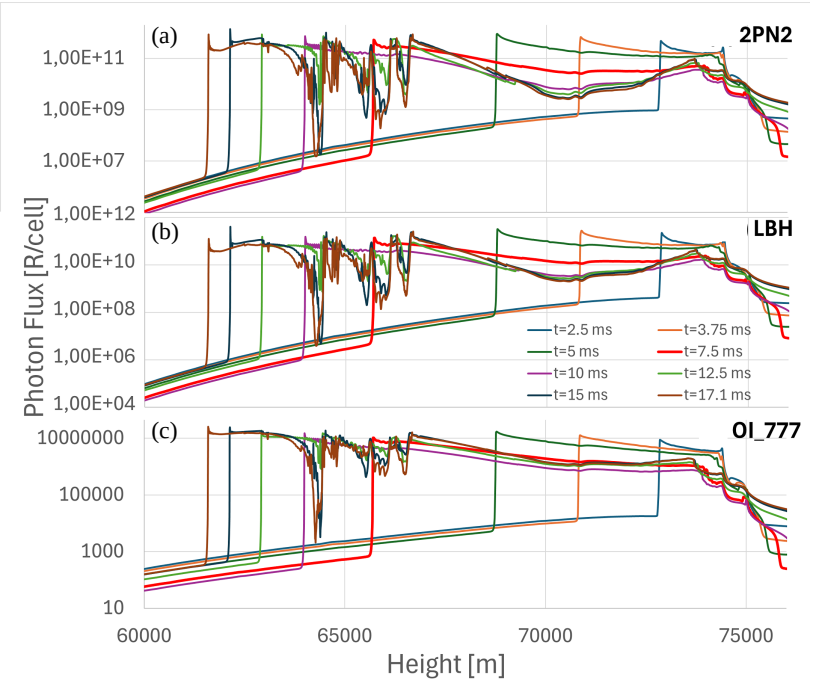


**FIGURE 7**. Vertical profiles of local photon flux for (a) $2PN_2$, (b) LBH ($N_2$), and (c) O I 777 nm at different times ($t = 2.5$–$17.1$ ms; colors indicated in the legend). The horizontal axis shows altitude in meters.

with the branch dynamics and front adjustment. However, the distance traveled by the bright region between successive times shortens, indicating front deceleration. To interpret this behavior, we introduced an effective luminous length for the head as follows:

$$L \sim v_{\text{head}}\,\tau_{\text{eff}}, \quad \tau_{\text{eff}} = \frac{1}{A+Q},$$

where the effective lifetime $\tau_{\text{eff}}$ [34] decreases as the head descends into denser layers (where $Q$ increases), while the head velocity $v_{\text{head}}$ decreases as it propagates in a weaker electric field owing to channel screening and less favorable background gradients [35]. The combined reduction of $\tau_{\text{eff}}$ and $v_{\text{head}}$ reduces $L$, so that the bright head region advances a shorter distance between successive times, as observed in the profiles.

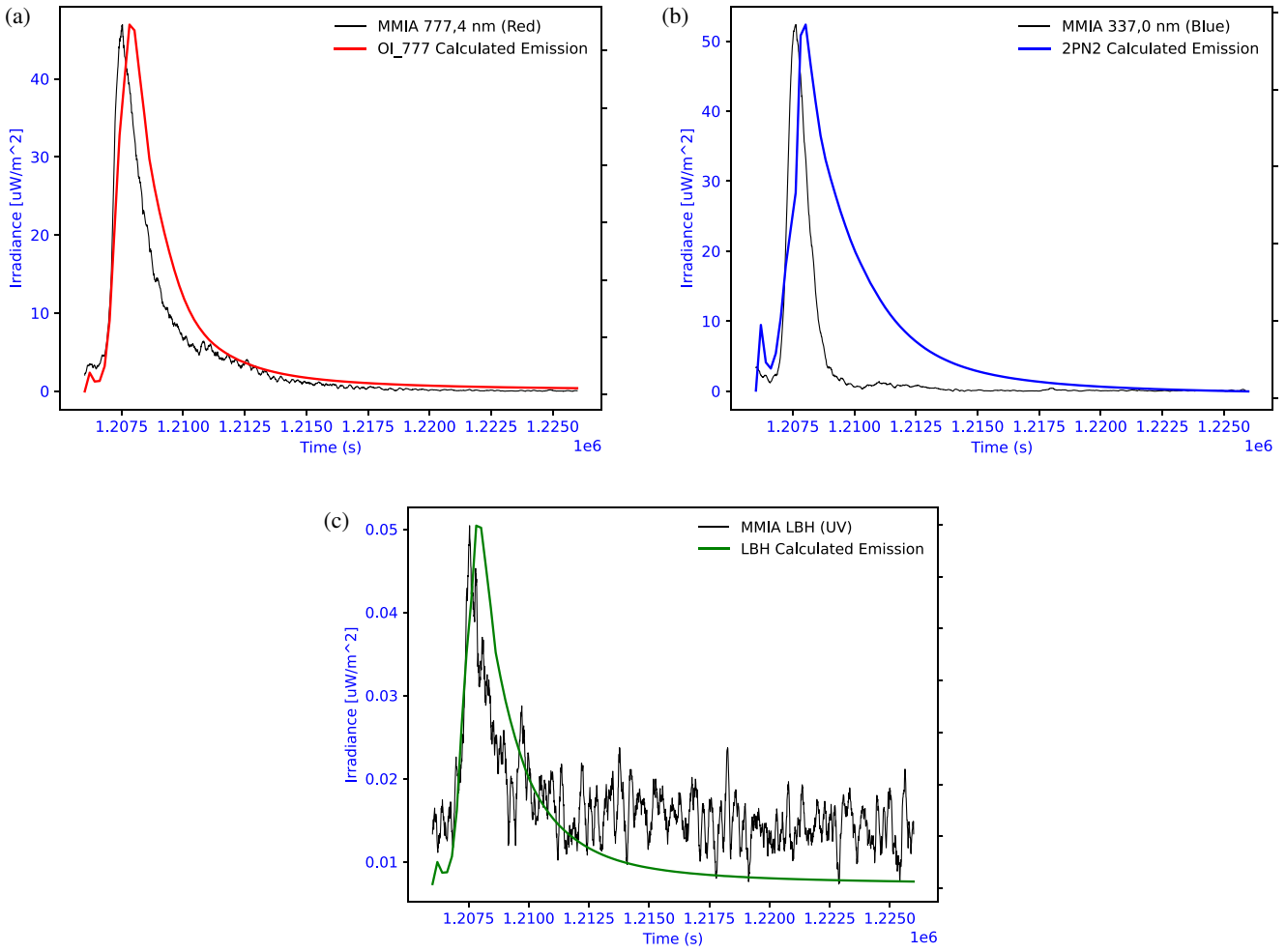


**FIGURE 8**. Model-observation comparison for `ASIM ID 51267`. (a) O I 777.4 nm: model (red) vs MMIA (black). (b) $2PN_2$ (337 nm): model (blue) vs MMIA (black). (c) LBH (FUV): model (green) vs MMIA (black).

### 3.4. Comparative Analysis of $2PN_2$, LBH, and O I 777 nm Spatial Profiles

The evolution of the emission in the remaining bands is shown in Fig. 7. In all three cases, a bright front descending over time is observed. The abrupt jump marks the streamer head. Above the front, a decaying plateau associated with the already formed channel appears, the level of which decreases mainly because of the reduction in $E/N$ and $n_e$ behind the head. Between ∼64 and 66.5 km, peaks and notches signal front branching, where the field is shared by multiple tips.

The differences between the bands are consistent with their specific physics. The $2PN_2$ band exhibited the highest levels and sharpest fronts, making it a good tracer of propagation. LBH reproduces the same overall morphology, but with slightly lower amplitudes, which is consistent with its greater sensitivity to losses and FUV absorption when atmospheric transmission is included. O I 777 nm emission, which is weaker and more localized, responds to the availability of atomic oxygen and the kinetics of $O(^5P)$, so its peaks can appear somewhat shifted to higher altitudes, where quenching is less efficient.

A common feature in all three panels is the reduction in peak displacement between successive times, indicating front deceleration once the formed channel screens part of the available field. This behavior can again be interpreted in terms of the effective luminous length $L \sim v_{\mathrm{head}}\tau_{\mathrm{eff}}$, which decreases as both the available field and head speed decrease.

### 3.5. Model-Observation Comparison

This section presents the light curves (Fig. 8) generated by applying the emission workflow to all simulation files (50 µs time steps, covering 0–17 ms). Excited-state populations were computed under QSS closure, local emissivity was derived, and nadir projection incorporated atmospheric transmittance (Rayleigh scattering in the visible/NIR region and significant $O_3$ absorption for LBH). The reported intensity is the brightness integrated over a region of interest, consistent with the ASIM-type metrics. These simulated light curves were compared with MMIA/ASIM observations for event ASIM ID 51267 on 6 June, 2021 at 02:00:30 UTC near Barrancabermeja (Colombia), which was used as a test case. For each spectral band (O I 777 nm, $2PN_2$ at 337 nm, and FUV LBH), the simulated

and measured signals were displayed side-by-side at the same cadence. The objective was to assess consistency in: (i) peak time and pulse width, (ii) tail morphology (quenching and/or continuing current), and (iii) relative amplitude across channels.

All channels showed a consistent temporal alignment of the main peak at ∼2–2.5 ms, indicating that the streamer/channel kinematics and viewing geometry were well captured by the model. The best absolute agreement is obtained for O I 777.4 nm (Fig. 8(a)), where both the peak time and decay closely match the observations. The $2PN_2$ emission reproduces the rise and maximum but exhibits a longer tail than observed (Fig. 8(b)), whereas the LBH band captures the initial peak but deviates at late times (Fig. 8(c)), where the satellite signal is dominated by noise and background.

The O I 777.4 nm agreement suggests that the modeled energy deposition and QSS treatment of the O($^5$P) level are adequate over the relevant $E/N$ range. The over-sustained $2PN_2$ tail points to uncertainties in effective quenching and cascade processes, whereas LBH discrepancies are consistent with background subtraction limits and simplified radiative transfer (pure absorption without scattering).

After this initial comparison, improved agreement across all channels was obtained by modest adjustments of selected model parameters (notably effective quenching rates and attenuation factors), without altering the underlying physical framework. This demonstrates that the emission workflow is robust and suitable for quantitative, event-by-event comparisons with ASIM photometer data.

## 4. DISCUSSION

The multispectral results obtained with the `Afivo Streamer` reproduced the characteristic features of mesospheric streamers. A brightness peak was co-located with the head (coincident maxima of $E/N$ and $n_e$), followed by a tail associated with the conductive channel. The spatial coincidence of the jumps in the four bands confirms that the common driver of emission is product $k(E/N)\,n_e$ at the streamer head. Differences in the level and slope among bands are explained by the radiative efficiency $A/(A+Q)$, by the target chemistry ($N_2$ vs. $O/O_2$), and, in the case of LBH, by atmospheric transmission $T_{\text{atm}}$. These mechanisms are directly reflected in ASIM/MMIA photometer observations, where all channels exhibit a temporally aligned main peak, indicating that the dominant contribution arises from the high-field head region rather than from the screened channel. In particular,

i) $2PN_2$ is the most sensitive tracer of the active zone owing to its higher $A$ and steep slope of $k(E/N)$,

ii) $1PN_2$ provides a robust and extended signal that is useful for visible-band instrumentation;

iii) LBH reproduces the $N_2$-based morphology but exhibits lower levels due to accumulated FUV absorption;

iv) O I 777.4 nm is concentrated at the head, with amplitude limited by the availability of atomic O and efficient quenching in dense layers.

The transition from a young, collimated front to a branched regime is evidenced by the appearance of multiple peaks and notches co-located between $2PN_2$ and LBH, consistent with field redistribution among sub-heads and channel screening. This pattern explains the reduction in the main peak after ∼10–15 ms and the shorter displacement between instants (deceleration). Small decreases in $E/N$ have a nonlinear impact on $k(E/N)$ and, therefore, on emissions. To quantify this evolution, we introduce a spatial scale associated with the optical extent of the head, the *effective luminous length*, defined as

$$L \sim v_{\text{head}}\,\tau_{\text{eff}}, \quad \tau_{\text{eff}} = \frac{1}{A+Q},$$

This provides a unified interpretation for the progressive compression of the bright region. As the discharge descends into denser layers, $\tau_{\text{eff}}$ decreases owing to increasing $Q$, and at the same time, the front decelerates because of screening and less favorable background field gradients. The combined reduction in $\tau_{\text{eff}}$ and $v_{\text{head}}$ reduces $L$ and explains why successive peaks appear closer together.

### 4.1. Implications for Observations

The co-localization of $2PN_2$/LBH peaks with $E/N$ maxima suggests that intensity ratios (e.g., $2PN_2/1PN_2$) can be used to diagnose $E/N$ and effective quenching, while O I 777.4 nm provides sensitivity to more energetic electron populations and atomic oxygen abundance. This interpretation is supported by ASIM comparisons, where the $2PN_2$ channel reproduces the timing of the observed peak but shows enhanced sensitivity to post-peak dynamics, whereas O I 777.4 nm exhibits the closest agreement in both peak timing and decay.

For comparison with ASIM, the FUV attenuation must be treated using realistic atmospheric profiles and the spectral response of the instrument. In particular, LBH observations are strongly affected by $O_2/O_3$ absorption and background subtraction uncertainties, which can dominate the late-time signal and must be accounted for before attributing discrepancies to plasma-chemical processes alone.

## 5. CONCLUSIONS

The multiband ($1PN_2$, $2PN_2$, LBH, and O I 777 nm) optical synthesis coupled with plasma modeling enabled consistent characterization of the spatial and temporal dynamics of the streamer. The emission maxima were concentrated at the head, where $E/N$ and $n_e$ maximized $k(E/N)$, producing a sharp peak that moved over time and a tail associated with the screened channel. The intensity order $2PN_2 > 1PN_2 >$ LBH $\gg$ O I is consistent with the excitation thresholds, quenching, and FUV absorption, and provides a framework for interpreting spectral contrasts. This hierarchy is consistent with the relative amplitudes measured by ASIM/MMIA for the analyzed event, reinforcing the validity of the modeled emission efficiencies and attenuation treatment.

The analysis reveals an initial intensification phase followed by a transition to a branched regime around ∼9.5 ms, evidenced

by multiple co-located peaks among $N_2$-based bands. Branching redistributes the electric field and electron density, decelerates the front, and generates multi-peak structures that are well captured by $2PN_2$, whereas LBH reproduces the morphology with a lower amplitude owing to FUV losses. The correlation between $1PN_2/2PN_2$ peaks, $|\mathbf{E}|$ structures, and $n_e$ variations confirmed the onset of branching and formation of sub-heads.

Intensity ratios (e.g., $2PN_2/1PN_2$) have emerged as sensitive diagnostics of $E/N$ and effective quenching, while O I 777.4 nm acts as a differential tracer for high-energy processes and atomic oxygen chemistry. Taken together, these results establish a quantitative basis for inferring the physical and chemical parameters of the discharge.

We developed a reproducible multiband optical synthesis framework that links plasma variables to the observed signals through $k(E/N)$, $A$, $Q$, and $T_{\text{atm}}$. The scheme is suitable for comparison with spaceborne instrumentation such as ASIM, provided that realistic atmospheric profiles are included to treat the FUV absorption and instrumental spectral response. The model-observation comparison presented here demonstrates that, after modest parameter adjustments within physically reasonable bounds, the same framework can reproduce the timing, pulse width, and relative channel behavior observed by ASIM.

This study consolidates a unified set of tools and metrics for studying streamer-type discharges and their transition to branched regimes, providing a robust basis for experimental validation and future extensions for full radiative transfer modeling.

## ACKNOWLEDGEMENT

This project was partially funded by a grant (Convocatoria Doctorados Nacionales 2016) from the former Administrative Department of Science, Technology and Innovation (Colciencias). I am sincerely grateful to this institution for its support.

Special thanks are given to the ASIM mission, particularly to Carol Anne Oxborrow, Torsten Neubert, Nikolai Østgaard, Victor Reglero, and other associated researchers. ASIM is a mission of the ESA SciSpace program for the scientific utilization of space exploration platforms, including the ISS and other space environment analogs. It is funded by the ESA and national contributions through contracts with TERMA and the Technical University of Denmark (DTU) in Denmark, the University of Bergen (UB) in Norway, and the University of Valencia (UV) in Spain.

## APPENDIX A. PLASMA FLUID SIMULATION

The electromagnetic simulation model implemented in `Afivo Streamer` uses a drift-diffusion-reaction fluid approach under the local field approximation, solving the continuity equations for electrons and ions coupled with Poisson's equation [6]. The simulation framework allows the dynamic allocation of computational resources through adaptive mesh refinement (AMR), which concentrates the resolution in regions with strong gradients of field and charge. A 2D axisymmetric domain and chemical scheme incorporating vibrational and electronic excitations, recombination, radiative decay, and quenching have been used [36].

### A.1. Computational Domain

The computational domain is shown in Fig. A1. It consists of a 2D axisymmetric cylindrical geometry that is used to simulate streamer growth. This type of domain is computationally efficient and well-suited for parametric studies and multispectral emission modeling. However, they are intrinsically less faithful than full 3D models in terms of streamer branching and mutual interactions.

As shown by Teunissen and Ebert [37], streamer branching arises from azimuthal instabilities that can only be captured in three-dimensional simulations. Comparative studies by Wang et al. [38, 39] further demonstrated that while 2D axisymmetric models can reproduce key macroscopic quantities, such as streamer velocity and head radius in non-branching regimes, they fail to qualitatively describe branching morphology, which is inherently three-dimensional.

In the present work, a 2D axisymmetric geometry is adopted to study the evolution of a dominant streamer channel and its associated multispectral optical emissions. The extension of the framework to fully 3D simulations, which are required to capture branching dynamics, is left for future work.

Figure A1 illustrates the spatial configuration of the computational domain in the $(r, h)$ plane, where $r$ is the radial coordinate, and $h$ is the altitude. The shaded gray area represents the physical domain bounded below by the ground and above by the ionosphere. A Gaussian plasma seed is initialized at an altitude of approximately 65 km, centered radially, with a vertical extent $H$ and radial width $R$, which serve as the input parameters to trigger the discharge. The simulation included a photoionization term. Although the model is 2D, the physical interpretation corresponds to a cylindrical system, in which all quantities are assumed to be invariant with respect to the azimuthal angle. The axisymmetric domain spans a radius of 5 km and a height of 30 km, covering the region from 50 to 80 km above sea level.

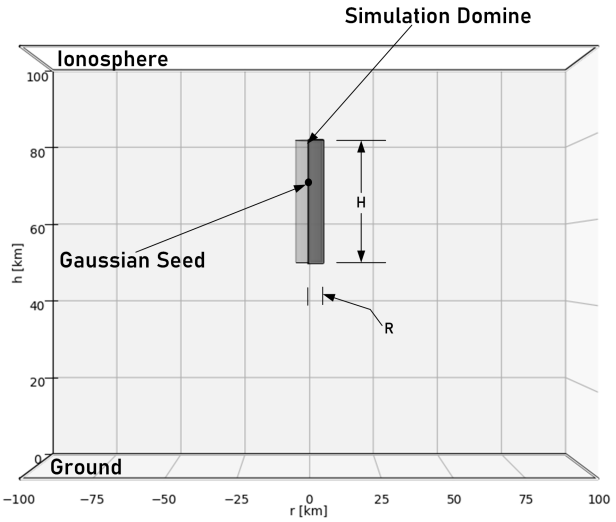


**FIGURE A1**. Geometric configuration of the domain for a 2D axisymmetric simulation of mesospheric discharges.

The simulation framework enables the dynamic allocation of computational resources via adaptive mesh refinement (AMR). As the streamer propagates, the grid recursively refines the cells, where the error indicators exceed the predefined thresholds. This produces a column of highly refined cells that follows the streamer head, consistently resolving the ionization channel width throughout its evolution. When space-charge branching occurs, the AMR algorithm adds additional refinement levels at each emerging tip while coarsening the upstream regions where the gradients decrease.

## REFERENCES


[1] Ihaddadene, M. A. and S. Celestin, "Determination of sprite streamers altitude based on $N_2$ spectroscopic analysis," *Journal of Geophysical Research: Space Physics*, Vol. 122, No. 1, 1000–1014, 2017.

[2] Chou, J. K., L. Y. Tsai, C. L. Kuo, Y. J. Lee, C. M. Chen, A. B. Chen, H. T. Su, R. R. Hsu, P. L. Chang, and L. C. Lee, "Optical emissions and behaviors of the blue starters, blue jets, and gigantic jets observed in the Taiwan transient luminous event ground campaign," *Journal of Geophysical Research: Space Physics*, Vol. 116, No. A7, 2011.

[3] Pérez-Invernón, F. J., A. Malagón-Romero, F. J. Gordillo-Vázquez, and A. Luque, "The contribution of sprite streamers to the chemical composition of the mesosphere-lower thermosphere," *Geophysical Research Letters*, Vol. 47, No. 14, e2020GL088578, 2020.

[4] Pasko, V. P., "Recent advances in theory of transient luminous events," *Journal of Geophysical Research: Space Physics*, Vol. 115, No. A6, 2010.

[5] Neubert, T., N. Ostgaard, V. Reglero, E. Blanc, O. Chanrion, C. A. Oxborrow, A. Orr, M. Tacconi, O. Hartnack, and D. D. V. Bhanderi, "The ASIM mission on the international space station," *Space Science Reviews*, Vol. 215, No. 2, 26, 2019.

[6] Teunissen, J. and U. Ebert, "Afivo: A framework for quadtree/octree AMR with shared-memory parallelization and geometric multigrid methods," *Computer Physics Communications*, Vol. 233, 156–166, 2018.

[7] Liu, N., V. P. Pasko, D. H. Burkhardt, H. U. Frey, S. B. Mende, H.-T. Su, A. B. Chen, R.-R. Hsu, L.-C. Lee, H. Fukunishi, and Y. Takahashi, "Comparison of results from sprite streamer modeling with spectrophotometric measurements by ISUAL instrument on FORMOSAT-2 satellite," *Geophysical Research Letters*, Vol. 33, No. 1, 2006.

[8] Luque, A. and U. Ebert, "Sprites in varying air density: Charge conservation, glowing negative trails and changing velocity," *Geophysical Research Letters*, Vol. 37, No. 6, 2010.

[9] Liu, N. and V. P. Pasko, "Molecular nitrogen LBH band system far-UV emissions of sprite streamers," *Geophysical Research Letters*, Vol. 32, No. 5, 2005.

[10] Pancheshnyi, S., S. Biagi, M. C. Bordage, G. J. M. Hagelaar, W. L. Morgan, A. V. Phelps, and L. C. Pitchford, "The LXCat project: Electron scattering cross sections and swarm parameters for low temperature plasma modeling," *Chemical Physics*, Vol. 398, 148–153, 2012.

[11] Bílek, P., T. C. Dias, V. Prukner, V. Guerra, and M. Simek, "Streamer-induced kinetics of excited states in pure $N_2$: II. Formation of $N_2(B^3\Pi_g, v = 0\text{–}21)$ through analysis of emission produced by the first positive system," *Plasma Sources Science and Technology*, Vol. 33, No. 1, 015011, Jan. 2024.

[12] Shibusawa, K. and M. Funatsu, "Radiative characteristics of $N_2$ first positive band in visible and near-infrared regions for microwave-discharged nitrogen plasma," *Transactions of the Japan Society for Aeronautical and Space Sciences*, Vol. 62, No. 2, 86–92, 2019.

[13] Gochitashvili, M. R., R. Y. Kezerashvili, and R. A. Lomsadze, "Excitation of Meinel and the first negative band system at the collision of electrons and protons with the nitrogen molecule," *Physical Review A*, Vol. 82, No. 2, 022702, 2010.

[14] Liu, N. and V. P. Pasko, "Effects of photoionization on propagation and branching of positive and negative streamers in sprites," *Journal of Geophysical Research: Space Physics*, Vol. 109, No. A4, 2004.

[15] Keilhauer, B., R. Engel, H. Klages, and T. Waldenmaier, "Nitrogen fluorescence yield in dependence on atmospheric conditions," in *Proceedings of the 29th International Cosmic Ray Conference*, Vol. 7, 119, Pune, India, 2005.

[16] Teunissen, J., "Improvements for drift-diffusion plasma fluid models with explicit time integration," *Plasma Sources Science and Technology*, Vol. 29, No. 1, 015010, 2020.

[17] Gordillo-Vázquez, F. J. and F. J. Pérez-Invernón, "A review of the impact of transient luminous events on the atmospheric chemistry: Past, present, and future," *Atmospheric Research*, Vol. 252, 105432, 2021.

[18] Chanrion, O., T. Neubert, I. L. Rasmussen, C. Stoltze, D. Tcherniak, N. C. Jessen, J. Polny, P. Brauer, J. E. Balling, S. S. Kristensen, *et al.*, "The modular multispectral imaging array (MMIA) of the ASIM payload on the international space station," *Space Science Reviews*, Vol. 215, No. 4, 28, 2019.

[19] Lepikhin, N. D., N. A. Popov, and S. M. Starikovskaia, "On electric field measurements based on intensity ratio of $1-$ and $2+$ systems of nitrogen in discharges with high specific deposited energy," *Plasma Sources Science and Technology*, Vol. 31, No. 8, 084002, Aug. 2022.

[20] Favre, A., M. Dimitrijevic, V. Morel, S. Djurovic, Z. Mijatovic, G. Godard, and A. Bultel, "Study of the 777 nm lines profile of atomic oxygen using laser-induced plasmas," *SCSLSA*, 2019.

[21] Stamnes, K., "Radiation transfer in the atmosphere: Ultraviolet radiation," in *Encyclopedia of Atmospheric Sciences*, 2nd ed., G. R. North, J. Pyle, and F. Zhang, Eds., 37-44, Academic Press, Oxford, 2015.

[22] Yoshino, K., W. H. Parkinson, K. Ito, and T. Matsui, "Absolute absorption cross-section measurements of Schumann-Runge continuum of $O_2$ at 90 and 295 K," *Journal of Molecular Spectroscopy*, Vol. 229, No. 2, 238–243, 2005.

[23] Stamnes, K., G. E. Thomas, and J. J. Stamnes, *Radiative Transfer in the Atmosphere and Ocean*, 2nd ed., Cambridge University Press, 2017.

[24] Liu, N., "Dynamics of positive and negative streamers in sprites," Ph.D. dissertation, The Pennsylvania State University, PA, USA, 2006.

[25] Caplinger, J. E. and G. P. Perram, "The importance of cascade emission and metastable excitation in modeling strong atomic oxygen lines in laboratory plasmas," *Plasma Sources Science and Technology*, Vol. 29, No. 1, 015011, 2020.

[26] Ebert, U., S. Nijdam, C. Li, A. Luque, T. Briels, and E. v. Veldhuizen, "Review of recent results on streamer discharges and discussion of their relevance for sprites and lightning," *Journal of Geophysical Research: Space Physics*, Vol. 115, No. A7, 2010.

[27] Nijdam, S., J. Teunissen, and U. Ebert, "The physics of streamer discharge phenomena," *Plasma Sources Science and Technology*, Vol. 29, No. 10, 103001, 2020.

[28] Liu, N., V. P. Pasko, H. U. Frey, S. B. Mende, H.-T. Su, A. B. Chen, R.-R. Hsu, and L.-C. Lee, "Assessment of sprite initiating electric fields and quenching altitude of $a^1\Pi_g$ state of $N_2$ using sprite streamer modeling and ISUAL spectrophotometric measurements," *Journal of Geophysical Research: Space Physics*, Vol. 114, No. A3, 2009.

[29] Pérez-Invernón, F. J., F. J. Gordillo-Vázquez, M. Passas-Varo, T. Neubert, O. Chanrion, V. Reglero, and N. Ostgaard, "Multispectral optical diagnostics of lightning from space," *Remote Sensing*, Vol. 14, No. 9, 2057, 2022.

[30] Baker, D. J., "Rayleigh, the unit for light radiance," *Applied Optics*, Vol. 13, No. 9, 2160–2163, 1974.

[31] Sentman, D. D., H. C. Stenbaek-Nielsen, M. G. McHarg, and J. S. Morrill, "Plasma chemistry of sprite streamers," *Journal of Geophysical Research: Atmospheres*, Vol. 113, No. D11, 2008.

[32] Gordillo-Vázquez, F. J., "Air plasma kinetics under the influence of sprites," *Journal of Physics D: Applied Physics*, Vol. 41, No. 23, 234016, Nov. 2008.

[33] Luque, A. and U. Ebert, "Growing discharge trees with self-consistent charge transport: The collective dynamics of streamers," *New Journal of Physics*, Vol. 16, No. 1, 013039, 2014.

[34] Stetson University, "Fluorescence lifetimes and dynamic quenching," ChemLibreTexts, [Online]. Available: https://tinyurl.com/fluor-lifetime, Mar. 2021.

[35] Li, J. and S. A. Cummer, "Measurement of sprite streamer acceleration and deceleration," *Geophysical Research Letters*, Vol. 36, No. 10, 2009.

[36] Malagón-Romero, A., A. Luque, N. S. Shuman, T. M. Miller, S. G. Ard, and A. A. Viggiano, "Associative electron detachment in sprites," *Geophysical Research Letters*, Vol. 51, No. 11, e2023GL107990, 2024.

[37] Teunissen, J. and U. Ebert, "Simulating streamer discharges in 3D with the parallel adaptive Afivo framework," *Journal of Physics D: Applied Physics*, Vol. 50, No. 47, 474001, 2017.

[38] Wang, Z., A. Sun, and J. Teunissen, "A comparison of particle and fluid models for positive streamer discharges in air," *Plasma Sources Science and Technology*, Vol. 31, No. 1, 015012, Jan. 2022.

[39] Wang, Z., A. Sun, and J. Teunissen, "A model comparison of 2D Cartesian and 2D axisymmetric models for positive streamer discharges in air," *arXiv preprint arXiv:2401.12353*, 2024.